(Received 18 September 2023, Accepted 26 December 2023, Scheduled 8 January 2024)

Two Approaches for Designing Circularly Polarized OAM Reflectarrays

Yuxuan Ding[1, 2], Yunhua Zhang[1, 2, *], and Xiaowen Zhao[1, 2]

[1] *CAS Key Laboratory of Microwave Remote Sensing*
National Space Science Center, Chinese Academy of Sciences, Beijing, China
[2] *The University of Chinese Academy of Sciences, Beijing, China*

ABSTRACT: By calculating the compensation phase distribution from the radiation fields of the feed, two approaches are proposed for reflectarrays (RAs) generating circularly polarized orbital angular momentum (CP-OAM) beams with higher mode purity. Particularly, if the radiation fields are extracted in spherical coordinates rather than Cartesian coordinates, the required phase distribution for generating a CP-OAM beam of $+1/-1$ mode can be directly obtained according to our mathematical derivation which shows that the spherical components of left-/right-hand circularly polarized (LHCP/RHCP) fields naturally involve the OAM phase term of $+1/-1$ mode. To better demonstrate our work, CP-OAM RAs with either smooth horn or corrugated horn of RHCP as feed are designed by three approaches: the conventional approach (CA) based on the estimated phase center, and two proposed approaches based on simulated radiation fields in Cartesian coordinates (CCA) and spherical coordinates (SCA), respectively. Full-wave simulation results show that the OAM mode purity can be enhanced by either CCA or SCA, and the SCA can produce even higher mode purities than CCA when an offset feed is employed.

1. INTRODUCTION

As a special kind of shaped beam, orbital angular momentum (OAM) beam can provide a new form of spatial multiplexing based on wavenumber and is of great potential in improving the transmission rate and channel capacity of communication systems. Faced with the reality that spectrum resources become increasingly scarce, the OAM multiplexing opens up a new way to further increase spectrum efficiency and reduce spectrum congestion [1]. The OAM property can also be applied to enhance the target recognition and imaging capabilities of radar systems [2]. Although the inherent beam divergence characteristic currently restricts the OAM to be only usable for short-distance peer-to-peer communications, many researchers have made progress in addressing the existing issues related to the OAM beam's short transmission distance [3, 4], poor reception [5, 6], as well as low mode purity [7–9].

As we know, reflectarray antenna (RA) and transmitarray antenna (TA) can be low-profile and lightweight, as they eliminate the need for feeding networks and expensive T/R modules, thereby enabling a cost-effective implementation of OAM beams [9–12]. Circular polarizations (CP) have the advantages of anti-polarization mismatch, anti-multipath, and are less affected by Faraday rotation. There are many approaches for designing circularly polarized OAM (CP-OAM) RA/TAs [12–14], among which the approach of adopting circular-polarized feed can significantly simplify the design of RA/TA elements [14–16].

Accurately extracting the feed illumination on the array elements is of utmost importance for designing RAs/TAs with better radiation performance [17–20]. Recently, when designing circularly polarized RA/TAs using circularly polarized feeds, the feed's radiation fields in Cartesian coordinates are extracted first, and further processing is undertaken to obtain the left-/right-hand circularly polarized (LHCP/RHCP) component of the field illuminated on each array element, i.e., the illumination field [17]. The compensation phase distribution for generating a pencil beam is then obtained via antenna array theory using the phases of the illumination field only [17, 19] or via optimization methods using the complex amplitudes of the illumination field [18, 20], wherein the latter is more accurate but time-consuming. However, to the best of the authors' knowledge, all current RA/TAs designed to generate OAM beams still rely on the estimated phase centers of the feeds when calculating compensation phase distributions. The conventional approach (CA) treats the feed's radiation as spherical waves originating from a virtual phase center, which is over-approximated and ultimately results in a degradation of OAM performance.

Mode purity is commonly used to evaluate the quality of the generated OAM beam [21–23]. Low mode purity means that the orthogonality between different OAM modes is poor, and as a result deteriorates the receiving signal-to-noise ratio (SNR) [24, 25]. In this letter, we propose and verify two approaches that, for the first time, calculate the compensation phase distribution of CP-OAM RAs according to the radiation fields of the feed, by which the mode purity of the generated CP-OAM beam can be improved compared to using CA. The first proposed approach is based on the radiation fields in Cartesian coordinates (CCA), while the second approach is more succinct utilizing the radiation fields in spherical coordinates (SCA). A rigorous derivation is conducted to validate the rea-

* Corresponding author: Yunhua Zhang (zhangyunhua@mirslab.cn).

sonableness of the SCA that arises from computational coincidence regarding the spherical components. To demonstrate the effectiveness of the proposed two approaches in improving the OAM mode purity, the CP-OAM RAs designed by CA, CCA, and SCA are simulated and compared.

2. THREE APPROACHES

Figure 1 shows the schematic setup for the CP-OAM RA, where three sets of coordinate systems are defined, i.e., the main (x, y, z) with the RA's aperture center as the origin, the horn (x', y', z') with the virtual phase center of the horn as the origin (z' points to the aperture center of the RA), and the element (x'', y'', z'') with the element position as the origin (x'' and y'' axes are on the array surface) [17]. The (x', y', z') on the array surface of $z = 0$ can be expressed by the coordinates (x, y, z):

$$\begin{cases} x' = -x\cos\theta_F \\ y' = y \\ z' = x\sin\theta_F + z_F\sec\theta_F \end{cases}, \tag{1}$$

where θ_F is the offset angle of the feed horn, and z_F is the height of the feed. The y-position of the feed $y_F = 0$, while its x-position $x_F = -z_F\tan\theta_F$.

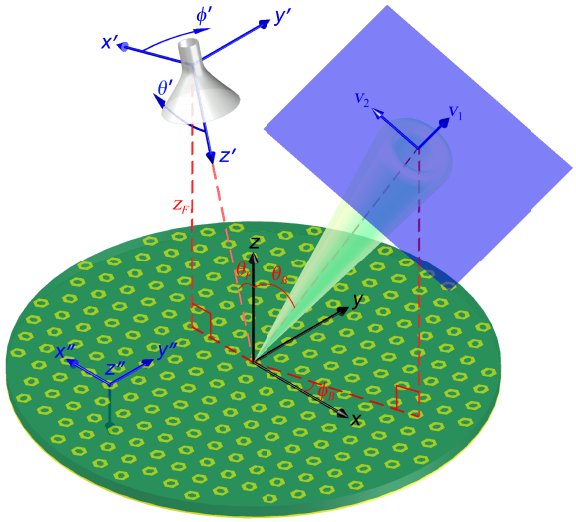

FIGURE 1. Configuration of the CP-OAM RA along with three coordinate systems.

The OAM mode purity is defined as follows [10, 26]:

$$\text{Purity} = W_{l_m} \Big/ \sum_{l=-\infty}^{\infty} W_l, \tag{2}$$

where

$$W_l = \int_0^{\rho_m} \left| \int_{-\pi}^{\pi} \Psi(\rho, \vartheta)\exp(-jl\vartheta)\, d\vartheta \right|^2 \rho\, d\rho \tag{3}$$

is the intensity of the l-order OAM mode, and l_m is the expected OAM mode. $\Psi(\rho, \vartheta)$ denotes the sampled phase on the sampling plane v_1-v_2 perpendicular to the propagation direction (θ_B, ϕ_B). $\rho = \sqrt{v_1^2 + v_2^2}$ and $\vartheta = \arctan(v_2/v_1)$ are the radial distance and polar angle of polar coordinates on the sampling plane, respectively. In our case, the circular sampling area with a radius $\rho_m = 150$ mm is 500 mm away from the aperture center of the RA.

In the following sections, CA is first introduced, and then CCA and SCA are introduced.

2.1. CA

In CA [9–16], the position of the approximate phase center of the feed is first fixed through simulation or measurement, and the illumination phases on the RA aperture are calculated according to the spatial phase delay from the phase center position to the element position. The pencil-beam phase distribution $\varphi_{\text{PB}}^{\text{CA}}(x, y)$ is then determined based on the antenna array theory:

$$\varphi_{\text{PB}}^{\text{CA}} = k_0 R' - k_0\sin\theta_B\left(x\cos\phi_B + y\sin\phi_B\right), \tag{4}$$

where $k_0 = 2\pi f_0/c$ is the free-space wavenumber at operating frequency f_0; R' is the distance from the phase center of the horn to the element position $(x, y, 0)$; and (θ_B, ϕ_B) is the desired beam direction.

An additional phase term $\varphi_l(x, y)$ is then superimposed onto this pencil-beam phase distribution to convert the spherical wavefront of the pencil beam to the helical wavefront of the OAM beam. That is, to generate an OAM beam directed at (θ_B, ϕ_B), the compensation phase for the element located at $(x, y, 0)$ can be expressed as:

$$\varphi_{\text{OAM}}^{\text{CA}} = \varphi_{\text{PB}}^{\text{CA}} + \varphi_l, \tag{5}$$

where $\varphi_l = l\arctan(y/x)$ and l is the OAM mode number.

Considering that most feeds do not have strictly spherical isophase surfaces and thus do not have a well-defined phase center, the compensation phases calculated using CA are not strictly accurate. Therefore, two approaches are proposed below to calculate the compensation phase distribution of CP-OAM RAs from the radiation fields of the feed.

2.2. CCA

The radiation field $(E_{x'}, E_{y'}, E_{z'})$ of a circularly polarized feed at every element position in Cartesian coordinates can be extracted via full-wave simulation or real measurement in an anechoic chamber. The transverse field components imposed on each array element are defined in the element coordinates, which can be obtained from $(E_{x'}, E_{y'}, E_{z'})$ via the following transformation:

$$\begin{pmatrix} E_{x''} \\ E_{y''} \\ E_{z''} \end{pmatrix} = \begin{pmatrix} \cos\theta_F & 0 & -\sin\theta_F \\ 0 & 1 & 0 \\ \sin\theta_F & 0 & \cos\theta_F \end{pmatrix} \begin{pmatrix} E_{x'} \\ E_{y'} \\ E_{z'} \end{pmatrix}. \tag{6}$$

Then we get the LHCP/RHCP component of the illuminated field:

$$E_{\text{L/R}}^{\text{CCA}} = E_{x''} \mp jE_{y''} = \cos\theta_F E_{x'} \mp jE_{y'} - \sin\theta_F E_{z'}, \tag{7}$$

where the subscripts L and R represent LHCP and RHCP, respectively.

Based on the antenna array theory, we can get the phase distribution $\varphi^{\mathrm{CCA}}_{\mathrm{PB,\,L/R}}(x,y)$ of the RA for generating a pencil beam pointing at (θ_B,ϕ_B):

$$\varphi^{\mathrm{CCA}}_{\mathrm{PB,\,L/R}} = -\arg\left(E^{\mathrm{CCA}}_{\mathrm{L/R}}\right) - k_0 \sin\theta_B \left(x\cos\phi_B + y\sin\phi_B\right), \quad (8)$$

where $\arg(E^{\mathrm{CCA}}_{\mathrm{L/R}})$ represents the phase of $E^{\mathrm{CCA}}_{\mathrm{L/R}}$.

As in CA, an OAM beam directed at (θ_B,ϕ_B) can be generated by adding the OAM phase term $\varphi_l(x,y)$ to the pencil-beam phase distribution. That is, the total phase distribution is:

$$\varphi^{\mathrm{CCA}}_{\mathrm{OAM,\,L/R}} = \varphi^{\mathrm{CCA}}_{\mathrm{PB,\,L/R}} + \varphi_l. \quad (9)$$

2.3. SCA

We propose to use the following (10) instead of (9) to calculate the phase distribution for generating a CP-OAM beam of mode $l=\pm1$ for the RA:

$$\varphi^{\mathrm{SCA}}_{\mathrm{L/R}} = -\arg\left(E^{\mathrm{SCA}}_{\mathrm{L/R}}\right) - k_0 \sin\theta_B \left(x\cos\phi_B + y\sin\phi_B\right), \quad (10)$$

where $E^{\mathrm{SCA}}_{\mathrm{L}} = E_{\theta'} - jE_{\phi'}$ and $E^{\mathrm{SCA}}_{\mathrm{R}} = E_{\theta'} + jE_{\phi'}$ are used in the LHCP case and RHCP case, respectively. The $E_{\theta'}$ and $E_{\phi'}$ are the spherical components of the feed's radiation fields extracted via full-wave simulation or real measurement. In the following, we shall show that if $E^{\mathrm{SCA}}_{\mathrm{L}}$ is used in (10), then the generated OAM beam will be of mode $+1$, while if $E^{\mathrm{SCA}}_{\mathrm{R}}$ is used, then the generated OAM beam will be of mode -1. Fig. 2 summarizes flowcharts of the CA, CCA, and SCA for a clearer comparison.

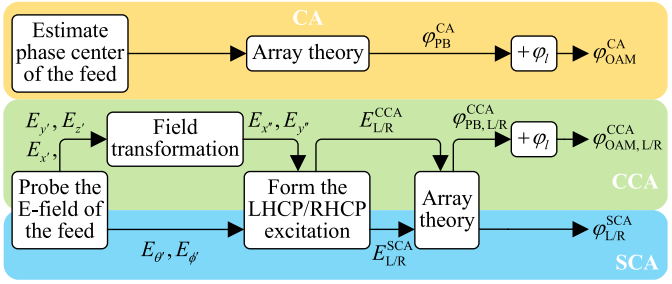

FIGURE 2. Flowcharts of the CA, CCA, and SCA.

2.4. Proof of the SCA

The relationship between the spherical components and Cartesian components of the electric field vector under far-field approximation is as follows:

$$\begin{cases} E_{\theta'} = \cos\theta'\cos\phi' E_{x'} + \cos\theta'\sin\phi' E_{y'} - \sin\theta' E_{z'} \\ E_{\phi'} = -\sin\phi' E_{x'} + \cos\phi' E_{y'} \end{cases}. \quad (11)$$

The $E^{\mathrm{SCA}}_{\mathrm{L/R}}$ in (10) can be reformulated using (11) as

$$E^{\mathrm{SCA}}_{\mathrm{L/R}} = E_{\theta'} \mp jE_{\phi'} = \left(\cos\theta'\cos\phi' \pm j\sin\phi'\right)E_{x'} + \left(\cos\theta'\sin\phi' \mp j\cos\phi'\right)E_{y'} - \sin\theta' E_{z'}. \quad (12)$$

And (12) can be rewritten as

$$E^{\mathrm{SCA}}_{\mathrm{L/R}} = w_{1,\mathrm{L/R}}E_{x'} + w_{2,\mathrm{L/R}}E_{y'} + w_3 E_{z'}, \quad (13)$$

where

$$\begin{cases} w_{1,\mathrm{L/R}} = \cos\theta'\cos\phi' \pm j\sin\phi' \\ w_{2,\mathrm{L/R}} = \cos\theta'\sin\phi' \mp j\cos\phi' \\ w_3 = -\sin\theta' \end{cases}, \quad (14)$$

and ϕ' is the azimuth angle in the feed coordinates, which can be calculated using (1):

$$\phi' = \arctan\frac{y'}{x'} = -\arctan\frac{y}{x\cos\theta_F}. \quad (15)$$

Similarly, (7) can be rewritten as

$$E^{\mathrm{CCA}}_{\mathrm{L/R}} = c_1 E_{x'} + c_{2,\mathrm{L/R}}E_{y'} + c_3 E_{z'}, \quad (16)$$

where

$$\begin{cases} c_1 = \cos\theta_F \\ c_{2,\mathrm{L/R}} = \mp j \\ c_3 = -\sin\theta_F \end{cases}. \quad (17)$$

For the sake of analysis, consider the following two approximations:

(i) The far-field components of a circularly polarized horn have the following approximate relationships: $E_{y'} \approx jE_{x'}$ for LHCP, and $E_{y'} \approx -jE_{x'}$ for RHCP.

(ii) Considering that the modulus of $E_{z'}$ is very small compared to $E_{x'}$ and $E_{y'}$, and is even smaller after being multiplied by $\sin\theta_F$ or $\sin\theta'$, the corresponding terms with respect to $E_{z'}$ are ignored in the following derivations.

Using these two approximations, the phase difference between $\varphi^{\mathrm{SCA}}_{\mathrm{L/R}}$ and $\varphi^{\mathrm{CCA}}_{\mathrm{PB,\,L/R}}$ can be derived as

$$\begin{aligned} &\varphi^{\mathrm{SCA}}_{\mathrm{L/R}} - \varphi^{\mathrm{CCA}}_{\mathrm{PB,\,L/R}} \\ &= -\arg\left(E^{\mathrm{SCA}}_{\mathrm{L/R}}\right) + \arg\left(E^{\mathrm{CCA}}_{\mathrm{L/R}}\right) \\ &= -\arg\left(\frac{w_{1,\mathrm{L/R}} + w_{2,\mathrm{L/R}}E_{y'}/E_{x'} + w_3 E_{z'}/E_{x'}}{c_1 + c_{2,\mathrm{L/R}}E_{y'}/E_{x'} + c_3 E_{z'}/E_{x'}}\right) \\ &\approx -\arg\left(\frac{w_{1,\mathrm{L/R}} \pm jw_{2,\mathrm{L/R}}}{c_1 \pm jc_{2,\mathrm{L/R}}}\right) \\ &= -\arg\left(w_{1,\mathrm{L/R}} \pm jw_{2,\mathrm{L/R}}\right) + \arg\left(c_1 \pm jc_{2,\mathrm{L/R}}\right), \end{aligned} \quad (18)$$

where

$$\begin{aligned} \arg\left(w_{1,\mathrm{L/R}} \pm jw_{2,\mathrm{L/R}}\right) &= \arg\left[\left(\cos\theta' + 1\right)\left(\cos\phi' \pm j\sin\phi'\right)\right] \\ &= \pm\phi' = \mp\arctan\frac{y}{x\cos\theta_F} \end{aligned} \quad (19)$$

and

$$\arg\left(c_1 \pm jc_{2,\mathrm{L/R}}\right) = \arg\left(\cos\theta_F + 1\right) = 0, \quad (20)$$

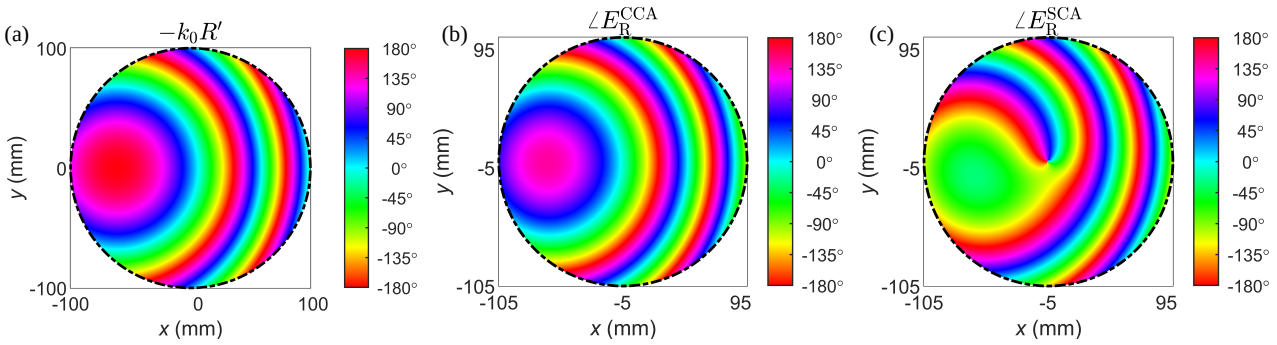

FIGURE 3. Illuminated phase distributions for the smooth-horn-fed RAs with $\theta_F = 15°$ calculated by (a) CA and (b) CCA. (c) Excitation phase distribution by SCA.

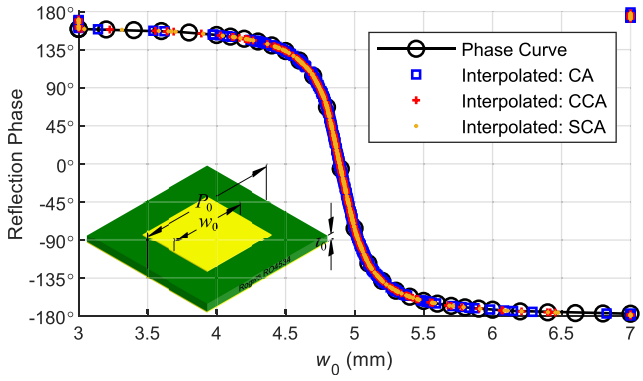

FIGURE 4. Phase curve of the square-latticed RA element from [22] and the interpolated phases required for three approaches. ($P_0 = 9.2$ mm and $t_0 = 0.51$ mm).

which gives

$$\varphi_{\mathrm{L/R}}^{\mathrm{SCA}} - \varphi_{\mathrm{PB,\,L/R}}^{\mathrm{CCA}} = \pm \arctan \frac{y}{x \cos \theta_F}. \tag{21}$$

When $\theta_F = 0°$, (21) becomes

$$\varphi_{\mathrm{L/R}}^{\mathrm{SCA}} - \varphi_{\mathrm{PB,\,L/R}}^{\mathrm{CCA}} = \pm \arctan \frac{y}{x}. \tag{22}$$

where the $+$ sign stands for LHCP, while the $-$ sign stands for RHCP.

This is consistent with the relationship in (9) converting a circularly polarized pencil beam to a CP-OAM beam, which means $\varphi_{\mathrm{L/R}}^{\mathrm{SCA}}$ is equal to $\varphi_{\mathrm{PB,\,L/R}}^{\mathrm{CCA}}$ when $l = \pm 1$. At this point, we can conclude that for an LHCP feed, if the spherical components of the feed's radiation fields are directly used to form the LHCP excitation $\varphi_{\mathrm{L}}^{\mathrm{SCA}}$, an OAM beam with $l = +1$ will be generated; while for an RHCP feed, an OAM beam with $l = -1$ will be generated using the RHCP excitation $\varphi_{\mathrm{R}}^{\mathrm{SCA}}$. In fact, we will show in the following examples that for small offset angles, e.g., $\theta_F = 15°$, the SCA can still generate satisfactory CP-OAM beams.

3. DESIGN EXAMPLES

In this section, the RHCP OAM RAs of mode $l = -1$ are designed by CA, CCA, and SCA separately. All RAs have an aperture diameter of 200 mm. Two common feed types, viz., a smooth horn antenna and a corrugated horn antenna, are used to feed the RA, both of which radiate a circularly polarized beam with 15 dBi gain at 15 GHz. Offset angles of $\theta_F = 0°$ (i.e., a prime-focus feed) and $\theta_F = 15°$ are experimented with for each feed, and the corresponding beam directions are $\theta_B = 0°$ and $\theta_B = 15°$, respectively. The other design specifications are as follows (refer to Fig. 1): the feed height $z_F = 230$ mm, the beam's azimuthal direction $\phi_B = 0°$, and the center frequency $f_0 = 15$ GHz.

First, the radiation fields of each feed are extracted using CST Studio Suite 2020, from which excitation phases $-k_0R'$, $\angle E_{\mathrm{R}}^{\mathrm{CCA}}$, and $\angle E_{\mathrm{R}}^{\mathrm{SCA}}$ are calculated by CA, CCA, and SCA, respectively, as presented in Fig. 3. Considering the limited paper length, only the results for the smooth horn with $\theta_F = 15°$ are presented in the figures.

To validate the effectiveness of the three approaches, three CP-OAM RAs of mode $l = -1$ are designed utilizing the polarization-insensitive element structure [22], with the smooth horn as the array's feed. Since the original RA element in [22] was designed for operation at 30 GHz, we rescale its dimensions to shift the center frequency to 15 GHz, and a dynamic phase range of approximately 336° is attained (which is larger than 325° as in [22]), as shown in Fig. 4, where w_0 in the inset is the side length of the square patch and P_0 is the element spacing. For a designed 200-mm-diameter array, a total of 333 elements are arranged in a square lattice with spac-

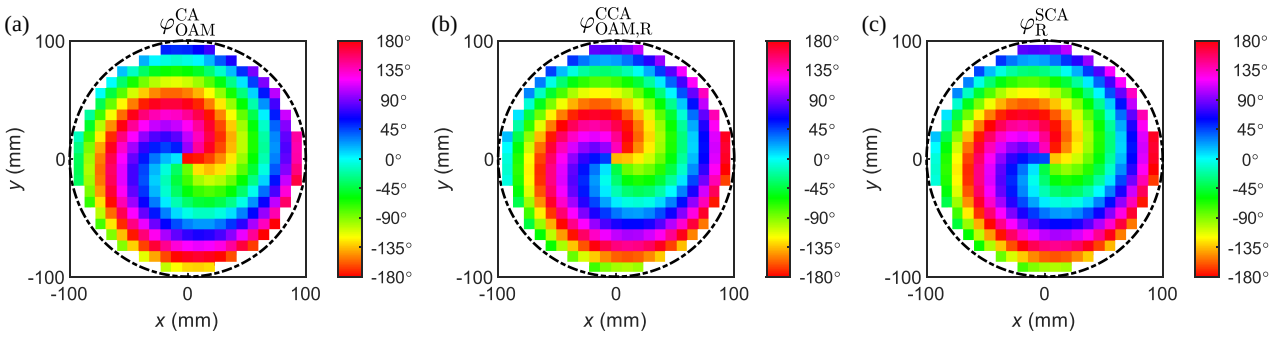

FIGURE 5. Compensation phase distributions calculated by three approaches for the smooth-horn-fed square-latticed CP-OAM RAs. (a) CA. (b) CCA. (c) SCA.

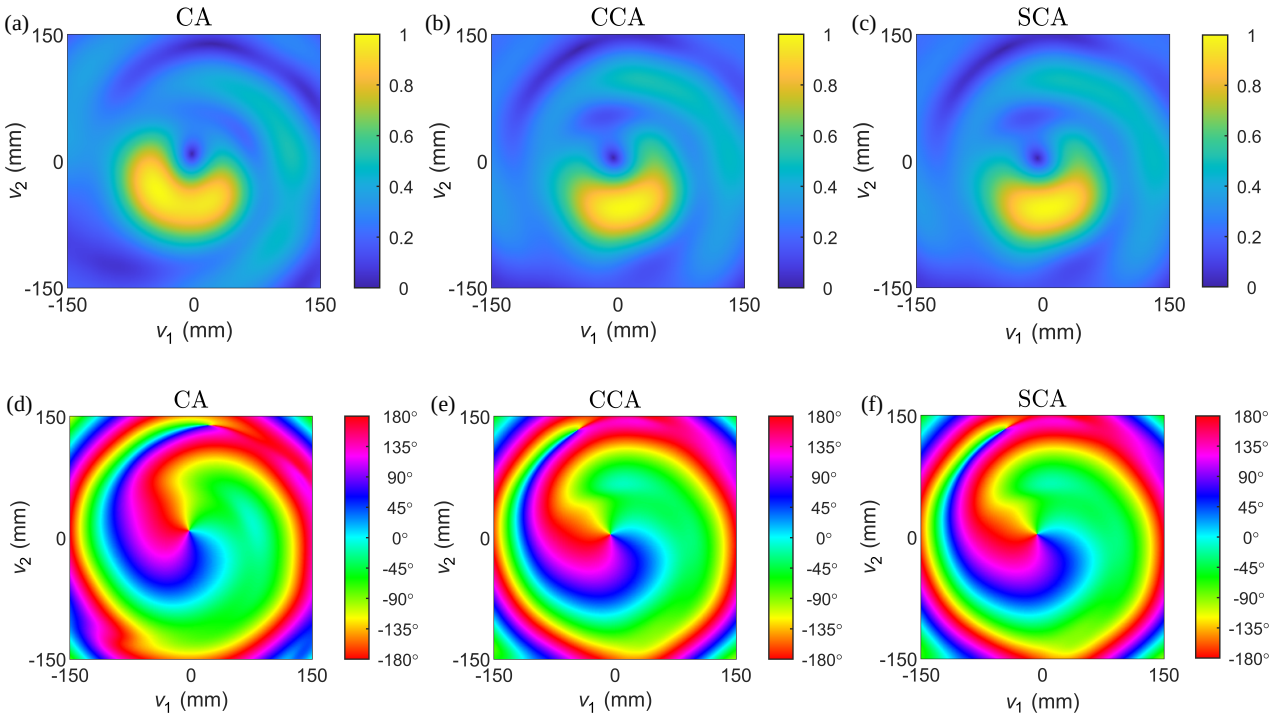

FIGURE 6. Simulated electric fields on the sampling plane radiated from the smooth-horn-fed square-latticed CP-OAM RAs. (a)–(c) Amplitude. (d)–(f) Phase.

ing $P_0 = 9.2\,\mathrm{mm}$. Next, (5), (9), and (10) are used to calculate compensation phases from the excitation phases $-k_0R'$, $\angle E_{\mathrm{R}}^{\mathrm{CCA}}$, and $\angle E_{\mathrm{R}}^{\mathrm{SCA}}$, respectively. An additional phase term $\varphi_{l=-1}(x,y)$ is then added in both CA and CCA. The final phase distributions $\varphi_{\mathrm{OAM}}^{\mathrm{CA}}(x,y)$, $\varphi_{\mathrm{OAM,\,R}}^{\mathrm{CCA}}(x,y)$, and $\varphi_{\mathrm{R}}^{\mathrm{SCA}}(x,y)$ are presented in Fig. 5.

Full-wave simulations are carried out using CST Studio Suite 2020 for three designed CP-OAM RAs. It should be noted that the handedness of the reflection wave from this element is opposite to the incidence wave, i.e., the reflected beam becomes LHCP when illuminated by RHCP feed. The near-field electric fields of the wavefront in the v_1-v_2 plane are then extracted and the OAM mode purity is calculated correspondingly using (2). The LHCP components of the electric fields are then calculated and presented in Fig. 6, as can be seen from which the spiral phases of the OAM wavefront of mode $l = -1$ are clearly shown. It is to say, all three approaches can generate the CP-OAM beam of mode $l = -1$ under the illumination of the RHCP feed. Detailed metrics are listed in Table 1, where we can see that CCA and SCA achieve higher mode purities than CA as expected. However, the mode purities are all below 55%, primarily due to the insufficient dynamic phase range of the simple element ($< 360°$), which inevitably produces more phase errors when forming the array. Additionally, the abrupt variation of patch geometry from element to element disrupts local periodicity, further damaging array performance [27].

In the following, a novel RA element is proposed based on the variable rotation technique (VRT) to enhance the mode purity and better exemplify the advantages of the proposed two approaches, as shown in Fig. 7, whose parameters are listed in Table 2. The Rogers RT5880 substrate with a dielectric constant of 2.2 and thickness of $0.787\,\mathrm{mm}$ has been adopted in the design. To minimize the complex mutual coupling between elements, the outer edge of the ring patch is kept unchanged, and only the inner edge is rotated according to the required compensation phase. The RHCP/LHCP reflection phase

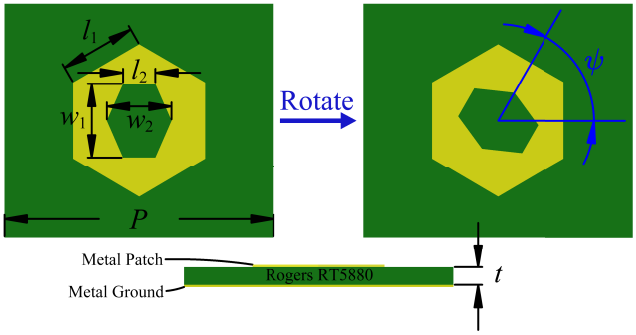

FIGURE 7. Geometry of the proposed equilateral-triangular-latticed RA element.

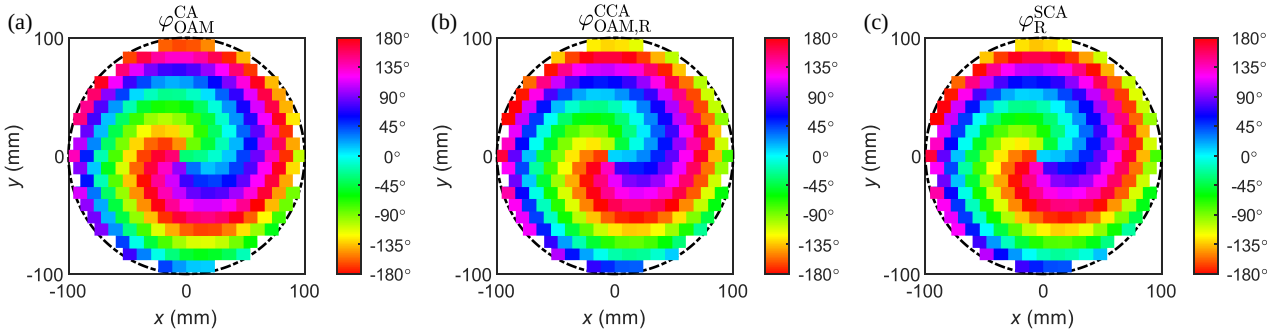

FIGURE 8. Compensation phase distributions calculated by three approaches for the smooth-horn-fed equilateral-triangular-latticed CP-OAM RAs with $\theta_F = 15°$. (a) CA. (b) CCA. (c) SCA.

TABLE 1. Performance comparison of the simulated CP-OAM RAs.

θ_F (θ_B)	Element Type	Feed Type	Approach	Peak Gain	Aperture Efficiency	Divergence Angle	Mode Purity
0°	[22]	Smooth	CA	20.49 dBi	11.34%	6.40°	49.78%
			CCA	20.34 dBi	10.96%	6.36°	53.39%
			SCA	20.28 dBi	10.81%	6.42°	52.82%
	Proposed	Smooth	CA	21.49 dBi	14.28%	5.37°	91.66%
			CCA	21.36 dBi	13.86%	5.63°	97.53%
			SCA	21.36 dBi	13.86%	5.56°	97.51%
		Corrugated	CA	21.43 dBi	14.08%	5.44°	97.25%
			CCA	21.35 dBi	13.83%	5.41°	98.83%
			SCA	21.38 dBi	13.92%	5.49°	98.75%
15°	Proposed	Smooth	CA	20.50 dBi	11.37%	5.03°	92.27%
			CCA	20.41 dBi	11.14%	5.38°	95.76%
			SCA	20.36 dBi	11.01%	5.64°	96.91%
		Corrugated	CA	21.40 dBi	13.99%	5.35°	95.83%
			CCA	21.35 dBi	13.83%	5.82°	97.92%
			SCA	20.96 dBi	12.64%	5.80°	98.32%

of the proposed element changes by $\pm 2\psi$ as the inner edge of the ring patch rotates by ψ, thereby achieving a dynamic phase range of 360°. Each 200-mm-diameter array comprises a total of 241 elements, arranged in an equilateral triangular lattice with spacing $P = 12$ mm. The compensation phase distributions $\varphi_{\mathrm{OAM}}^{\mathrm{CA}}(x, y)$, $\varphi_{\mathrm{OAM,\,R}}^{\mathrm{CCA}}(x, y)$, and $\varphi_{\mathrm{R}}^{\mathrm{SCA}}(x, y)$ are presented in Fig. 8.

Using the proposed reflective element along with the smooth horn and the corrugated horn as feed, CP-OAM RAs with phase distributions calculated by CA, CCA, and SCA are implemented separately. Full-wave simulations are carried out using CST Studio Suite 2020 for 12 RAs corresponding to two feeds, two offset angles, and three different approaches. The RHCP near fields on the v_1-v_2 plane are visualized in Fig. 9. Compared to Fig. 6, the amplitude distributions in Fig. 9 are much

TABLE 2. Dimension parameters of the proposed equilateral-triangular-latticed RA element.

P	t	l_1	l_2	w_1	w_2
12 mm	0.787 mm	3.4 mm	1.45 mm	3.3 mm	2.9 mm

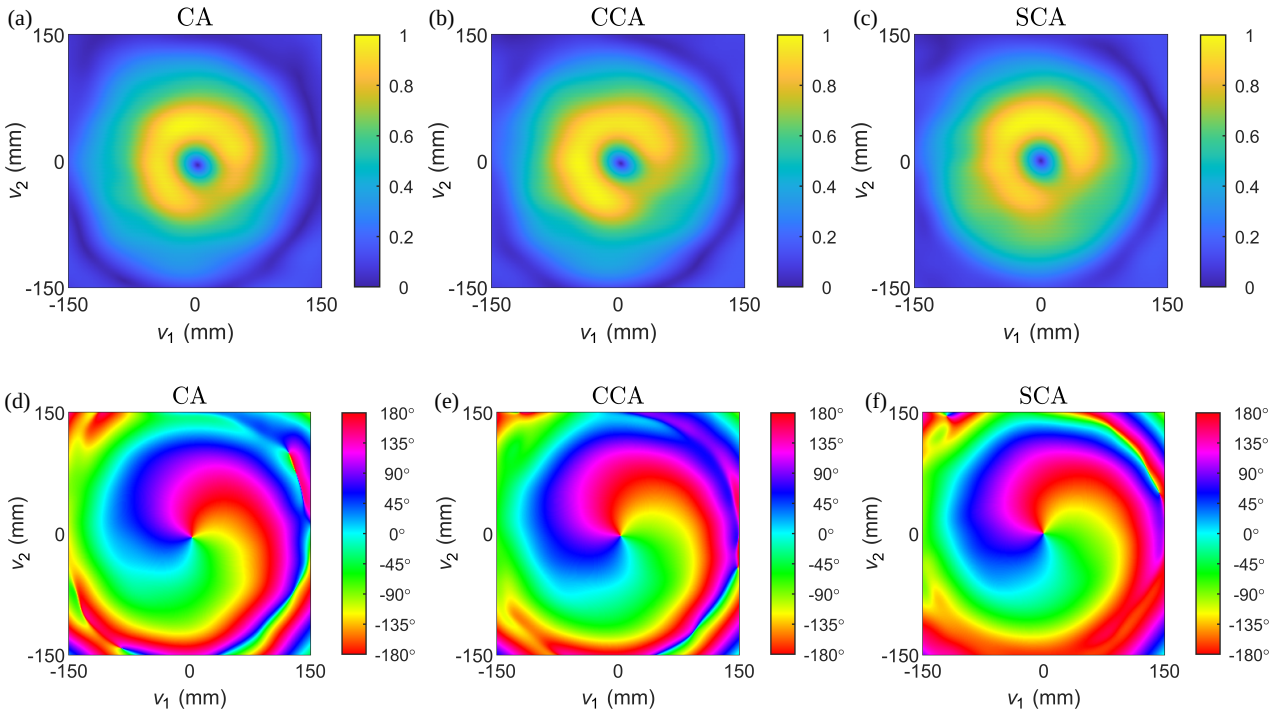

FIGURE 9. Simulated electric fields on the sampling plane radiated from the smooth-horn-fed equilateral-triangular-latticed CP-OAM RAs with $\theta_F = 15°$. (a)–(c) Amplitude. (d)–(f) Phase.

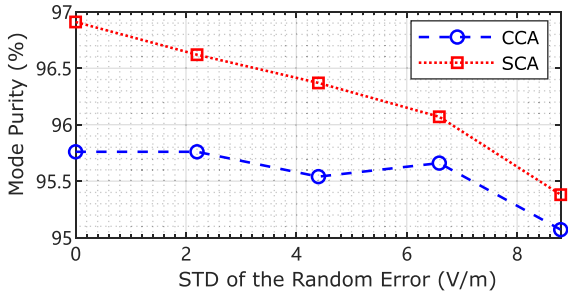

FIGURE 10. Mode purities of the smooth-horn-fed CP-OAM RAs by CCA and SCA after adding random errors with different standard deviations (STD) to the extracted components.

closer to full rings, and the phase transition is much smoother as well. Fig. 9(f) also demonstrates that the SCA still performs well at the 15° offset angle, as further evidenced by the achieved OAM mode purities summarized in Table 1.

In fact, we can further draw some conclusions from Table 1:

(i) For both horns with both 0° and 15° offset angles, the OAM mode purity can be improved by either CCA or SCA as compared to CA.

(ii) The mode purity improvement by CCA or SCA is more significant for the smooth-horn feed than for the corrugated-horn feed, and is most significant for the smooth-horn feed with no offset. This is because the phase center uncertainty of the smooth horn is larger than that of the corrugated horn, which is in accordance with the antenna theory. Moreover, the impact of uneven illuminated amplitude distribution is minimal when fed without offset.

(iii) The corrugated horn performs better than the smooth horn benefitting from its more uniform amplitude distribution of the illuminated field over the RA aperture.

(iv) In the $\theta_F = 0°$ case, CCA achieves slightly higher mode purities than SCA, and the small differences mainly come

from the approximation error of SCA, i.e., the two approximations that make SCA equivalent to CCA; while in the $\theta_F = 15^\circ$ case, the mode purities of CCA are inferior to that of SCA, and this is because the extraction error of the $E_{z'}$ component [28] in CCA is greater than the approximation error of SCA.

To test the error-tolerant abilities of CCA and SCA, we deliberately add random noise following a complex normal distribution to the $E_{x'}$, $E_{y'}$, $E_{z'}$, $E_{\theta'}$, and $E_{\phi'}$ extracted from the smooth horn. Specifically, the added noise has a mean of 0, and a standard deviation (STD) ranging from 5% to 20% of the averaged field amplitude over the aperture, which is about 42.93 V/m. Compensation phase distributions of CCA and SCA are then calculated from the modified Cartesian components and spherical components, respectively, which are used to implement smooth-horn-fed CP-OAM RAs. The results, as shown in Fig. 10, indicate that the mode purity of both CCA and SCA decreases as the STD of the added Gaussian noise increases, and they gradually get closer to each other. Moreover, although the purity of SCA declines faster than that of CCA, the former is consistently larger than the latter within the test range.

4. CONCLUSION

To improve the mode purity of OAM beams, this paper proposes to use the phase directly from the illuminated electric field to calculate the compensation phase for CP-OAM RAs, and two approaches are proposed, viz., CCA and SCA, which use the Cartesian components and the spherical components of the feed's radiation field, respectively. The SCA is derived from an interesting finding that the spherical components per se of a circularly polarized feed involve the OAM phase term of mode $+1/-1$, so the compensation phase distribution for generating an LHCP/RHCP OAM beam of mode $+1/-1$ can be directly obtained from the radiated spherical components of the feed.

The feasibility of the proposed approaches has been verified through full-wave simulations, from which the following main outcomes can be obtained:

(i) The mode purity of CP-OAM RAs with either a prime-focus feed or an offset feed can be enhanced by either CCA or SCA.

(ii) The mode purity improvement is more significant for those feeds whose radiation fields are more different from ideal spherical waves.

(iii) The process of the SCA is more concise than the CCA, and in some cases, SCA can obtain better results than CCA because of the smaller extraction error associated with spherical field components as opposed to Cartesian field components.

Obviously, element design has a major impact on the performance of CP-OAM RAs. A good element structure can bring the well-designed phase distribution into full play. The simulated mode purities of CP-OAM beams designed by the proposed CCA/SCA combined with the proposed element exceed 98% for corrugated-horn-fed cases, which are remarkably higher than those achieved by OAM RA/TAs in other works [9–11, 22, 23].

Although the above designs of CP-OAM RAs are based on full-wave simulations of the feed's radiated electric field, the proposed approaches are also applicable to real measured electric fields from different measurement systems, e.g., the near-field scanning system [29] or the far-field measurement system [17], in cases where the feed model for simulation is not available. Finally, we should point out that since the TA is based on the same phase compensation principle as the RA except that its beam is generated in the lower hemisphere ($\theta > 90^\circ$), the proposed approaches are also applicable to TA for generating the CP-OAM beam.

REFERENCES

[1] Zhang, W., S. Zheng, X. Hui, R. Dong, X. Jin, H. Chi, and X. Zhang, "Mode division multiplexing communication using microwave orbital angular momentum: An experimental study," *IEEE Transactions on Wireless Communications*, Vol. 16, No. 2, 1308–1318, Feb. 2017.

[2] Liu, K., Y. Cheng, Y. Gao, X. Li, Y. Qin, and H. Wang, "Super-resolution radar imaging based on experimental OAM beams," *Applied Physics Letters*, Vol. 110, No. 16, 164102, Apr. 2017.

[3] Ge, X., R. Zi, X. Xiong, Q. Li, and L. Wang, "Millimeter wave communications with OAM-SM scheme for future mobile networks," *IEEE Journal on Selected Areas in Communications*, Vol. 35, No. 9, 2163–2177, Sep. 2017.

[4] Yu, L., X. Li, Z. Qi, H. Zhu, Y. Huang, and Z. Akram, "Wideband circularly polarized high-order bessel beam reflectarray design using multiple-ring-cascade elements," *IEEE Antennas and Wireless Propagation Letters*, Vol. 19, No. 7, 1226–1230, Jul. 2020.

[5] Chen, R., W.-X. Long, X. Wang, and J. Li, "Multi-mode OAM radio waves: Generation, angle of arrival estimation and reception with UCAs," *IEEE Transactions on Wireless Communications*, Vol. 19, No. 10, 6932–6947, 2020.

[6] Zhang, C., X. Jiang, and D. Chen, "Signal-to-noise ratio improvement by vortex wave detection with a rotational antenna," *IEEE Transactions on Antennas and Propagation*, Vol. 69, No. 2, 1020–1029, Feb. 2021.

[7] Ma, J., X. Song, Y. Yao, Z. Zheng, X. Gao, and S. Huang, "Research on the purity of orbital angular momentum beam generated by imperfect uniform circular array," *IEEE Antennas and Wireless Propagation Letters*, Vol. 20, No. 6, 968–972, Jun. 2021.

[8] Liu, D., W. Wu, L. Gui, and T. Jiang, "OAM mode purity improvement based on antenna array," *Digital Communications and Networks*, Jan. 2023.

[9] Akram, Z., X. Li, Z. Qi, A. Aziz, L. Yu, H. Zhu, X. Jiang, and X. Li, "Broadband high-order OAM reflective metasurface with high mode purity using subwavelength element and circular aperture," *IEEE Access*, Vol. 7, 71 963–71 971, 2019.

[10] Shahmirzadi, A. V. and A. A. Kishk, "OAM carrying vortex beam mode interconversion using modular cascaded transmitarrays," *IEEE Transactions on Microwave Theory and Techniques*, Vol. 70, No. 7, 3591–3605, Jul. 2022.

[11] Huang, H.-F. and S.-N. Li, "High-efficiency planar reflectarray with small-size for OAM generation at microwave range," *IEEE*

Antennas and Wireless Propagation Letters, Vol. 18, No. 3, 432–436, Mar. 2019.

[12] Chen, G.-T., Y.-C. Jiao, and G. Zhao, "A reflectarray for generating wideband circularly polarized orbital angular momentum vortex wave," *IEEE Antennas and Wireless Propagation Letters*, Vol. 18, No. 1, 182–186, Jan. 2019.

[13] Veysi, M., C. Guclu, F. Capolino, and Y. Rahmat-Samii, "Revisiting orbital angular momentum beams: Fundamentals, reflectarray generation, and novel antenna applications," *IEEE Antennas and Propagation Magazine*, Vol. 60, No. 2, 68–81, Apr. 2018.

[14] Ahmed, Z., A. Muhammad, S. Kausar, and M. B. Ihsan, "Dual circularly polarized all-metal orbital angular momentum beam reflectarray antenna," in *2022 IEEE International Symposium on Antennas and Propagation and USNC-URSI Radio Science Meeting (AP-S/URSI)*, 581–582, Jul. 2022.

[15] Wang, Y., K. Zhang, Y. Yuan, X. Ding, B. Ratni, S. N. Burokur, and Q. Wu, "Planar vortex beam generator for circularly polarized incidence based on FSS," *IEEE Transactions on Antennas and Propagation*, Vol. 68, No. 3, 1514–1522, Mar. 2020.

[16] Li, J.-S. and L.-N. Zhang, "Simple terahertz vortex beam generator based on reflective metasurfaces," *Optics Express*, Vol. 28, No. 24, 36 403–36 412, Nov. 2020.

[17] Arrebola, M., Y. Álvarez, J. A. Encinar, and F. Las-Heras, "Accurate analysis of printed reflectarrays considering the near field of the primary feed," *IET Microwaves, Antennas & Propagation*, Vol. 3, No. 2, 187–194, Mar. 2009.

[18] Zhou, M., S. B. Sørensen, O. S. Kim, S. Pivnenko, and G. Toso, "Investigations on accurate analysis of microstrip reflectarrays," in *33rd ESA Antenna Workshop on Challenges for Space Antenna Systems*, 18–21, Oct. 2011.

[19] Smith, T., U. Gothelf, O. S. Kim, and O. Breinbjerg, "Design, manufacturing, and testing of a 20/30-GHz dual-band circularly polarized reflectarray antenna," *IEEE Antennas and Wireless Propagation Letters*, Vol. 12, 1480–1483, 2013.

[20] Budhu, J. and A. Grbic, "Perfectly reflecting metasurface reflectarrays: Mutual coupling modeling between unique elements through homogenization," *IEEE Transactions on Antennas and Propagation*, Vol. 69, No. 1, 122–134, Jan. 2021.

[21] Xue, W., X. Chen, H. Shi, H. Huang, J. Chen, and A. Zhang, "Evaluation of the purity of OAM modes using the reverberation chamber technique," in *2020 14th European Conference on Antennas and Propagation (EuCAP 2020)*, 1–4, Copenhagen, Denmark, Mar. 2020.

[22] Ali, A., M. Khalily, T. Brown, and R. Tafazolli, "Beam-steering capability for OAM-based reflectarray at 5G-mmwave frequencies," *IET Microwaves, Antennas & Propagation*, Vol. 17, No. 2, 162–168, Feb. 2023.

[23] Rao, M. V., J. Malik, S. Yuvaraj, and M. V. Kartikeyan, "Polarization insensitive reflectarray for OAM beam generation over octave bandwidth for 5G applications," *AEU - International Journal of Electronics and Communications*, Vol. 170, 154775, Oct. 2023.

[24] Zhang, J., G. Zhu, J. Liu, X. Wu, J. Zhu, C. Du, W. Luo, Y. Chen, and S. Yu, "Orbital-angular-momentum mode-group multiplexed transmission over a graded-index ring-core fiber based on receive diversity and maximal ratio combining," *Optics Express*, Vol. 26, No. 4, 4243–4257, 2018.

[25] Drysdale, T. D., B. Allen, C. Stevens, S. J. Berry, F. C. Smith, and J. Coon, "How orbital angular momentum modes are boosting the performance of radio links," *IET Microwaves, Antennas & Propagation*, Vol. 12, No. 10, 1625–1632, 2018.

[26] Yao, E., S. Franke-Arnold, J. Courtial, S. Barnett, and M. Padgett, "Fourier relationship between angular position and optical orbital angular momentum," *Optics Express*, Vol. 14, No. 20, 9071–9076, Oct. 2006.

[27] Moustafa, L., R. Gillard, F. Peris, R. Loison, H. Legay, and E. Girard, "The phoenix cell: A new reflectarray cell with large bandwidth and rebirth capabilities," *IEEE Antennas and Wireless Propagation Letters*, Vol. 10, No. 1, 71–74, 2011.

[28] Schejbal, V. and J. Hönig, "Holographic method of near-field antenna measurements," in *1980 10th European Microwave Conference*, 167–171, 1980.

[29] Rioult, J., S. Delgrande, N. Bremard, G. Copin, and V. Deniau, "Autonomous electromagnetic mapping system in augmented reality," in *2019 International Symposium on Electromagnetic Compatibility (EMC EUROPE 2019)*, 138–143, Barcelona, Spain, Sep. 2019.